Canadian Journal of Earth Sciences

OPEN ACCESS | Article

Evaluation of carbon dioxide sequestration via interaction with peridotite and peridotite-hosted groundwaters: an experimental case study with Bay of Islands Ophiolite rocks, western Newfoundland, Canada

M.J. Gill[a], **K.M. Poduska**[b], **and P.L. Morrill**[a]

[a]Memorial University, Department of Earth Sciences, St. John's, NL, Canada; [b]Memorial University, Department of Physics and Physical Oceanography, St. John's, NL, Canada

Corresponding author: **P.L. Morrill** (email: pmorrill@mun.ca)

Abstract

This study measured the CO_2 gas flux into various aqueous media (i.e., simulated ultra-basic and basic groundwater, and deionized water) containing ultramafic rock. Basic and ultra-basic waters simulated the aqueous chemistry and ion concentrations of distinct groundwaters found within terrestrial ultramafic bodies. Experiments were performed in a closed chamber in-line with a CO_2 analyzer, which measured the gaseous CO_2 concentration in the chamber every second. Total inorganic carbon, as well as aqueous species Ca, Mg, and Si were monitored in the reaction fluids. All three fluid types sequestered CO_2. The addition of crushed peridotite to deionized water reduced the CO_2 concentration in the headspace by 70 ppm ($\pm$9 ppm, 1σ, $n = 3$) and had a calculated CO_2 flux of -2.5×10^4 mol/m^{2}min ($\pm 9 \times 10^5$ mol/m^{2}min, 1σ, $n = 3$), while the greatest CO_2 flux was observed in ultra-basic Ca-rich waters of -1.40×10^3 mol/m^{2}min ($\pm 3 \times 10^5$ mol/m^{2}min, 1σ, $n = 3$), which reduced the headspace CO_2 concentration by 323 ppm ($\pm$4 ppm, 1σ, $n = 3$). The presence of calcite was detected using FTIR in ultra-basic waters in the presence and absence of ultramafic rock. A carbon mass balance model indicated that solid carbonates were precipitated in the ultra-basic water experiments, converting up to 59% of the CO_2 removed from the chamber headspace in 4 h. Extrapolating the data collected in these experiments, it was estimated that at surface conditions, with an adequate residence time, the mass of ultramafic rock in the Bay of Islands Complex in Newfoundland could sequester up to 4 million tonnes of atmospheric CO_2.

Key words: Carbon mineralization, carbon sequestration, CO_2 flux, ultramafic rock, serpentinization, surficial CO_2 removal (CDR), carbon storage

Introduction

The exponential rise in global atmospheric CO_2 from 280 ppm in 1750 to 409 ppm in 2020 should be cause for concern (NOAA 2020). The rise has been confidently linked to anthropogenic influences that increase globally every year (Knorr 2009). The high levels of CO_2 are associated with climate change, including an increase in global mean temperatures, severe weather events, and destruction/disruption of biological processes (Solomon et al. 2009). There are two primary methods for mitigating the increasing level of atmospheric CO_2 concentrations: reducing the amount of carbon emissions emitted to the atmosphere and removing carbon from the atmosphere at an accelerated rate via CO_2 sequestration.

CO_2 sequestration refers to any active process that removes CO_2 from the atmosphere. The focus of this study is on surficial carbon dioxide removal (CDR) paired with carbon mineralization. This process is found to occur naturally in ultramafic rock where CO_2 is removed directly from the air and mineralized as solid carbonate (Kelemen et al. 2018, 2020). Primary igneous minerals (i.e., olivine and pyroxene) and their hydrous counterparts (i.e., serpentine group minerals and brucite) provide the chemical components necessary to form carbonates such as calcite and magnesite (Paukert et al. 2012).

Ophiolites are exposures of ultramafic rock in terrestrial environments that possess a high capacity for CO_2 sequestration. Ophiolites are preserved sections of oceanic crust and upper mantle emplaced onto continental margins, exposing them subaerially. When exposed at Earth's surface, ultramafic minerals are out of equilibrium and are therefore highly reactive. The reactivity of ophiolites leads to the process of serpentinization (Eq. 1). At terrestrial sites of serpentinization, high pH groundwaters are observed (Barnes et al. 1967; Paukert et al. 2012; Giampouras et al. 2020, Szponar et al. 2013).

In the near surface of an ophiolite, minerals such as brucite and chrysotile dissolve, enriching the groundwater in Mg.

This process either produces hydroxide ions (Eq. 2) or consumes hydrogen ions (Eq. 3), buffering the waters to a pH ~10. These waters are referred to as Type I waters (Barnes and O'Neil 1969; Kelemen and Matter 2008; Paukert et al. 2012). At a pH of 10, surface waters readily dissolve gaseous CO_2, which speciates to bicarbonate (HCO_3^-) and carbonate (CO_3^{2-}) (Eq. 4). The Type I waters can infiltrate the ophiolite via fractures and faults to a depth where they become isolated from the atmosphere. During this process, magnesite precipitation occurs, which depletes that water of Mg^{2+} (Eq. 5). These waters then dissolve Ca-rich minerals, such as augite and diopside, due to the mineral's instability at low temperature ($T < 150$ °C) and low Si-activity. During the dissolution of Ca-rich minerals, the water is buffered to an ultra-basic pH of 12 and enriched in Ca^{2+} (Eq. 6) (Frost and Beard 2007). Additional Mg from the dissolution of diopside precipitates as magnesite in the subsurface (Eq. 5). The Ca^{2+}- and OH^--enriched waters are known as Type II water (Paukert et al. 2012). When Type II groundwaters discharge at the surface, where they are in contact with the atmospheric CO_2, they precipitate Ca carbonate (Eq. 7).

(1) $$\underset{\text{Fayalite}}{Fe_2SiO_4} + 5\underset{\text{Forsterite}}{Mg_2SiO_4} + 9H_2O \rightarrow 3\underset{\text{Serpentine}}{Mg_3Si_2O_5(OH)_4} + \underset{\text{Brucite}}{Mg(OH)_2} + \underset{\text{Iron(II)hydroxide}}{2Fe(OH)_2}$$

(2) $$\underset{\text{Brucite}}{Mg(OH)_2} \leftrightarrow Mg^{2+}{}_{(aq)} + 2OH^-{}_{(aq)}$$

(3) $$\underset{\text{Chrysotile}}{Mg_3Si_2O_5(OH)_4} + 6H^+{}_{(aq)} \leftrightarrow 3Mg^{2+}{}_{(aq)} + 2SiO_{2(aq)} + 2H_2O$$

(4) $$CO_2 + H_2O \leftrightarrow H_2CO_{3(aq)} \leftrightarrow \underset{\text{Bicarbonate}}{HCO^-_{3(aq)}} + H^+{}_{(aq)} \leftrightarrow \underset{\text{Carbonate}}{CO^{2-}_3{}_{(aq)}} + H^+{}_{(aq)}$$

(5) $$Mg^{2+}{}_{(aq)} + CO^{2-}_3{}_{(aq)} \leftrightarrow \underset{\text{Magnesite}}{MgCO_3}$$

(6) $$\underset{\text{Diopside}}{3CaMgSi_2O_6} + 12H^+{}_{(aq)} \leftrightarrow 3Ca^{2+}{}_{(aq)} + 3Mg^{2+}{}_{(aq)} + 6H_2O + 6SiO_{2(aq)}$$

(7) $$Ca^{2+}{}_{(aq)} + CO^{2-}_3{}_{(aq)} \leftrightarrow \underset{\text{Calcite}}{CaCO_3}$$

As such, these reactions demonstrate that atmospheric carbon can be sequestered both in the subsurface as Mg carbonate and at surface as Ca carbonate, making ophiolites very promising sites for industrial carbon sequestration projects. The specific fluid–rock reaction pathways are not fully understood, and the sequestration potential of several ophiolites, such as the Bay of Islands Ophiolite, remains unexplored. More work is needed to determine the water–rock–atmosphere interactions occurring with ultramafic rock and associated groundwaters. This work will contribute to determining the CO_2 flux associated with simulated basic and ultra-basic groundwaters and the effect of ultramafic rock on CO_2 flux.

Several CO_2 mineralization pilot projects are underway such as the Wallula Basalt Pilot Project in Washington, USA, and the CarbFix Project in Kopavogur, Iceland. These projects are both performed in mafic formations. While these projects have been successful (Pogge von Strandmann et al. 2019; White et al. 2020), ultramafic rocks are significantly more chemically reactive than their mafic counterparts in subaerial environments and therefore could more rapidly mineralize carbonates. Surficial carbon dioxide removal (CDR) is the process of reacting CO_2 bearing air and surface waters with reactive rocks to produce carbonates. Compared to other methods of CO_2 mineralization, surficial CDR is relatively low cost, as it requires little energy input. However, large surface areas and volume of rock are required (Kelemen et al. 2020).

In this study, we measured the CO_2 sequestration capacity of ultramafic ophiolitic rock using an experimental approach which quantifies CO_2 fluxes and fluid–rock chemical interactions. Newfoundland, Canada, hosts many ophiolites including the Bay of Islands Complex (BOIC), the Great Bend Ophiolite, and the Central Advocate Ophiolite Complex. Carbon dioxide sequestration experiments were conducted in closed batch reactors to quantify the CO_2 flux of BOIC rocks. This reactor simulated the water–rock–atmosphere interactions occurring at ambient pressures and temperatures in natural systems.

Materials and methods

Geologic setting

The Bay of Islands Ophiolite Complex (BOIC) is located on the west coast of Newfoundland, Canada. The complex is divided into four massifs each roughly 20 km in diameter. From south to north, the massifs are Lewis Hills, Blow Me Down (BMD), North Arm, and Tablelands (Fig. 1). The BOIC represents the only complete ophiolite sequence in the Appalachians consisting of, from bottom to top, ultramafic tectonites, ultramafic and mafic cumulates, massive gabbro, sheeted dikes, and pillow basalts (DiPietro 2013). The ultramafic cumulates are composed of dominantly harzburgite with dunite lenses and pyroxenite dikes. Below the cumulates, the ultramafic tectonite layer is composed of foliated harzburgite and lherzolite with minor websterite bands (Girardeau and Nicolas 1981). The complex was emplaced onto the Laurentian rift margin as the forearc of an oceanic arc that collided with the continental margin (Elthon 1991; Van Staal et al. 2007). This collision at 470 Ma signified the initial closure of the Iapetus Ocean known as the Taconic orogeny (Staal et al. 2007). This orogenic event subaerially exposed the ultramafic rocks forming the ophiolite complex.

Sample collection and preparation

Hand samples (~10–30 cm in maximum dimension) were collected from the talus slopes of BMD with approximate coordinates of 21 U 409883 m E, 5429804 m N. When selecting rock samples, the extent of weathering was considered (i.e., samples that had the least amount of weathering were chosen). Samples that exhibited the highest angularity were selected as the extent of transport was minimal and primary outcrops were buried in talus. The collected samples had their exterior weathered edges removed using a rock saw, this ensured that minimally oxidized peridotite was used in the experiments. Subsequently, samples were crushed using

Fig. 1. Sampling location within the Bay of Islands Complex (BOIC) in western Newfoundland. Ultramafic plutonic rock are purple and mafic plutonic rock are orange. The yellow stars on the satellite image represent approximate locations where samples were collected. Compiled with QGIS using lithology boundaries obtained from the Geoscience Atlas of Newfoundland and Labrador (Geological Survey Newfoundland and Labrador 2013) and satellite imagery from Google Maps. Map projection: NAD 83 Zone 21.

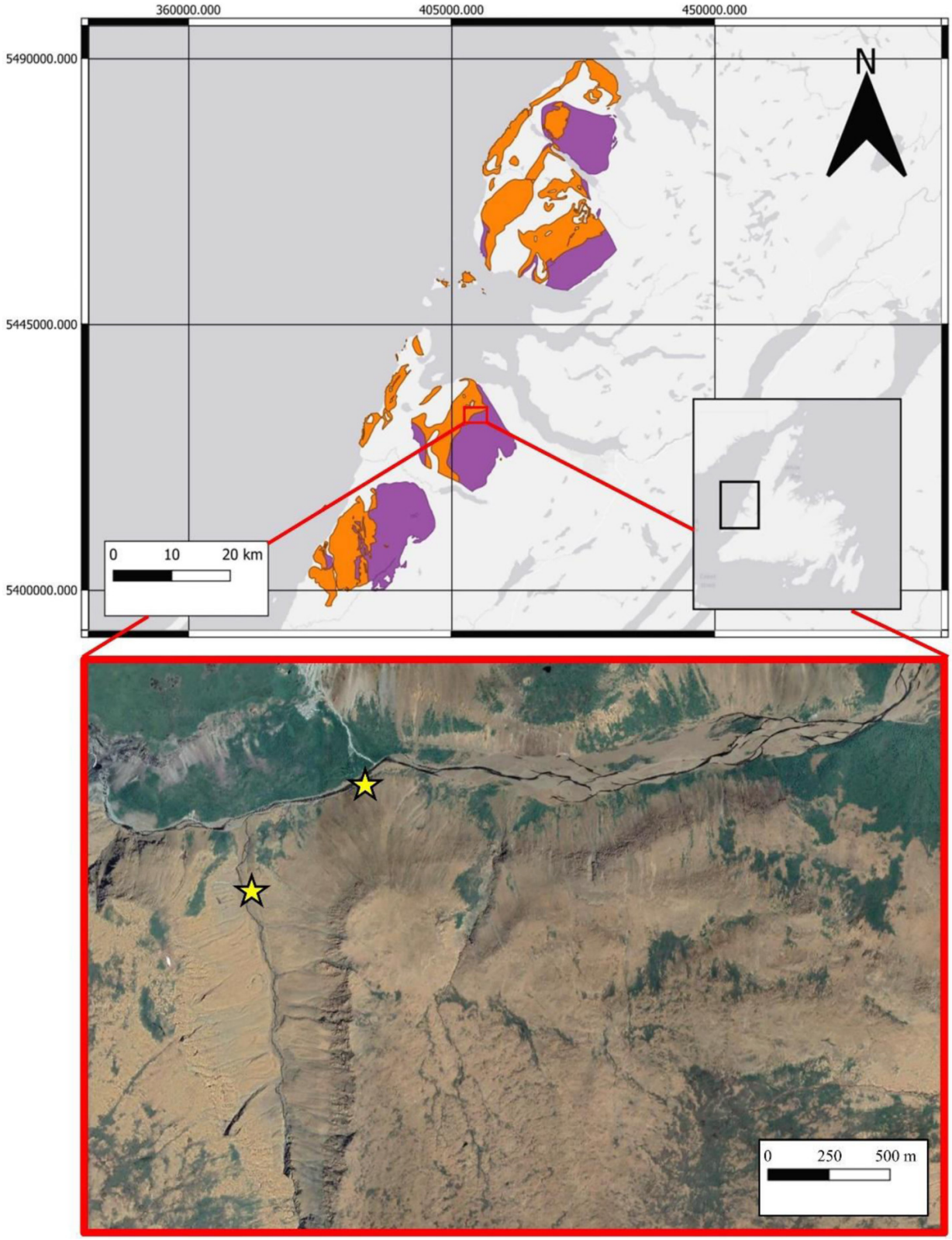

a jaw crusher and a disk mill. The rocks were then sieved to a diameter of <0.7 cm to remove the larger fraction.

Experimental approach

A total of 18 experiments were carried out in a gas flux chamber connected to a CO_2 analyzer. Three different fluid types were used: deionized water, basic water, and ultra-basic water. The basic and ultra-basic waters were used to simulate the aqueous chemistry of Type I and Type II peridotite-hosted groundwaters. For each reaction fluid type, two distinct experimental trials were conducted to evaluate CO_2 sequestration and flux, as a function of fluid–rock interaction: (i) an initial trial performing measurements in the presence of reaction fluid only (i.e., control) and (ii) a trial employing reaction fluid with crushed peridotite from BMD. Each experiment was completed in triplicate for reproducibility. Basic waters (pH ~10) were created by adding 0.1 g of $Mg(OH)_2$ to 1 L of deionized water, and ultra-basic waters (pH ~12) were created by adding 0.1 g of $Ca(OH)_2$ to 1 L of deionized water. After the solute was dissolved, the waters were sparged with nitrogen gas for 5 min to remove aqueous inorganic carbon (e.g., CO_2, HCO_3^-) from solution. Basic and ultra-basic waters were created to simulate Type I and Type II waters, respectively. For each experiment, 300 mL of the chosen reaction fluid was placed under a CO_2 survey chamber with or without the addition of 300 g of crushed peridotite. The measurement started with a 30 s dead band before closing the chamber, followed by another 30 s dead band after the chamber closed. These dead bands allowed CO_2 concentrations to stabilize. Subsequently, the chamber remained closed for 240 min. Gaseous CO_2 concentrations were analyzed every second of the experiment.

Conductivity and pH of the fluids were measured before and after each experiment. Additional experiments were also performed using end-member pH fluids (i.e., deionized water and ultra-basic water) in the presence of ultramafic rock in which the pH and conductivity were recorded every 15 min. Time series experiments were not performed on basic waters as previous experiments observed little change in pH between the start and end of the experiments. Aqueous samples were taken before and after each experiment for total inorganic carbon (TIC) and ion concentration analysis (Ca, Mg, Si). TIC samples were collected in 24 mL volatile organic analysis (VOA) vials with no headspace. The vials were sealed with black butyl septa. Samples taken for ion concentration analysis were collected in polypropylene centrifuge tubes using a 0.45 μm mixed cellulose ester (MCE) filter. A solid white film was observed on the surface of the reaction fluids for some of the experiments. This film was collected on glass microfiber filters (GF/F) and analyzed using a Fourier Transform Nano Infrared Spectrometer (FTIR).

Analytical methods

Sample characterization

Thin sections were created from each rock sample and analyzed using a Nikon Eclipse polarizing microscope. Thin section photomicrographs were taken using a Lumenera Infinity 3 camera with Infinity Analyze software. Thin sections were analyzed using a 2011 model FEI Quanta FEG 650 scanning electron microscope (SEM) equipped with a dual Bruker EDS detector in the Micro Analysis Facility (MAF) CREAIT Laboratory at Memorial University of Newfoundland. Mineral Liberation Analysis (MLA) software was used to discriminate and identify individual mineral grains using backscattered electron (BSE) images. This method determined modal mineral composition for each thin section. BSE images were captured using XT microscope server software. An operating voltage of 25 kV and a beam current of 10 nA were used. The working distance between sample and detector was 13.5 mm. The imaging scan speed was 16 μs with a resolution of 500 pixels.

Powdered rock samples were analyzed in the Earth Resources Research and Analysis Facility (TERRA) CREAIT laboratory at Memorial University of Newfoundland. Powdered samples were mounted in side-pack mounts to randomly orient mineral grains. X-Ray diffraction (XRD) analysis was performed on powdered rock samples using a Rigaku XtaLAB Synergy-S X-Ray diffractometer paired with a HyPix X-Ray detector to identify mineral phases in the sample. Grain size distribution was determined for a 300 g sample using sieve grain size analysis. A W.S. Tyler Ro-Tap sieve shaker was used with seven different sieve diameters between 4000 μm and 63 μm. Three hundred grams of sample were loaded into the top sieve and shaken for 1 h to ensure complete sieving of the sample. Samples from each size fraction were weighed using an analytical balance. Assuming that all grains were spherical, the volume per grain in each size fraction was determined using the median grain size in each fraction as the sphere's diameter. The total volume of each size fraction was divided by the volume per grain to determine the total number of grains in each size fraction. For a conservative estimate, the surface area of a sphere (i.e., minimum surface area possible for a particle) in each size fraction was determined and multiplied by the number of grains to give the minimum total surface area for the sample.

Gaseous CO_2 concentrations

The Li-Cor 8100–103 survey chamber was connected to the Li-Cor 8100 A CO_2 analyzer and control unit. During each experiment, the crushed peridotite and reaction fluid were placed inside the survey chamber (Fig. 2). From the control unit, a 30 s pre-purge was initiated to allow the gaseous headspace to equilibrate with surrounding atmosphere and then the chamber was sealed. The flux chamber had a diameter of 20 cm and a volume of 4823.9 cm^3, which was connected to the control unit via inlet and outlet gas tubes. Gases flowed from the inlet tube through a filter into the control unit where gaseous CO_2 concentrations were measured by a non-destructive infrared gas analyzer. The gas was then returned to the chamber via an outlet valve, which created constant air circulation between the control unit and survey chamber. Prior to experiments, a CO_2 scrubber (soda lime) was used to zero the infrared gas analyzer. The CO_2 scrubber was inserted onto the inlet line which removed CO_2 from the air before it reached the infrared analyzer. Once CO_2 concentrations stabilized, the analyzer was zeroed.

Fig. 2. Experimental set-up of the Li-Cor soil flux system. The Li-Cor 8100–003 survey chamber (A) is placed on top of the soil collar (B) to create a closed system. Within the soil collar (B), the reaction fluid is combined with crushed peridotite. The Li-Cor 8100–103 survey chamber (A) is connected to the Li-Cor 8100 A analyzer unit (D) via inlet, outlet, and bellow lines (C). The gas inlet and outlet lines maintain constant air circulation between the analyzer and survey chamber. The direction of gas flow is indicated by blue arrows. The bellows line allows the survey chamber to close and open at the start and end of an experiment.

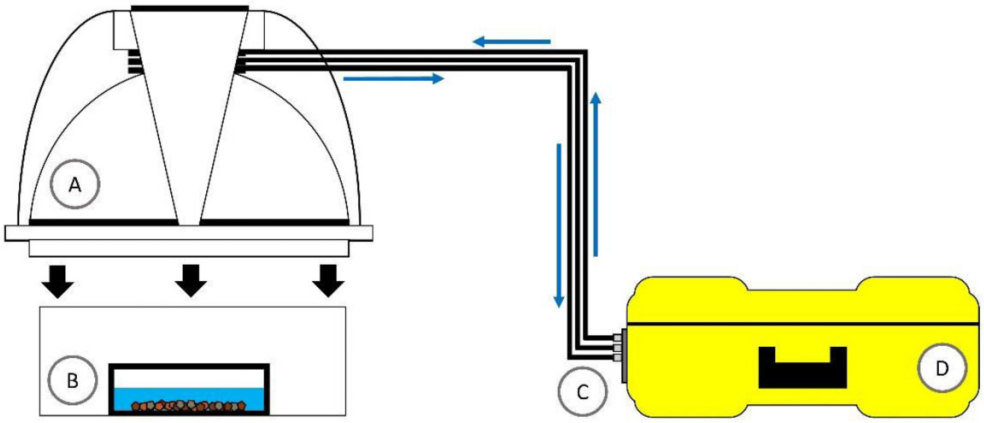

The CO_2 analyzer is accurate to 1.5% of the measured value (https://www.licor.com/env/products/soil_flux/LI-8100a).

Aqueous geochemistry measurements

Conductivity and pH of the reaction fluids were measured using a ThermoScientific Orion Star A conductivity cell and pH electrode. The pH electrode was calibrated using pH 4.01, 7.00, 10.01, and 12.46 buffers. The conductivity cell was calibrated using 100 μs/cm, 1413 μs/cm, and 12.9 mS/cm standards. The pH probe and conductivity cell had precisions, as reported by the manufacturers, of ±0.03 and ±0.3 μs/cm, respectively.

TIC was measured at the Biogeochemistry of Boreal Ecosystems Research Group Laboratory (BBERG) at Memorial University of Newfoundland using a Shimadzu TOC-VCPH coupled with Shimadzu ASI-V autosampler. Two hundred microliters of sample were acidified using phosphoric acid (samples with a pH higher than 10.5 were pre-acidified using hydrochloric acid). The gaseous headspace of the acidified sample was then injected into a furnace combusted at a temperature of 720 °C, which was then measured by a nondispersive infrared sensor (NDIR). The analyzer had a precision of ±3%.

Dissolved element concentrations in experimental fluids were analyzed with a Perkin Elmer Optima 5300 DV inductively coupled plasma-optical emission spectrometer (ICP-OES) housed in the MAF at Memorial University of Newfoundland. Acid-matrix blanks and solution calibration standards were measured throughout the experiment, bracketing sample unknowns, to allow for both calibration of blank-corrected emission line intensities and drift correction. For method data quality assessment, two measurements of the SCP Science EnviroMATTM ground water reference material ES-H-2 were prepared as per supplier recommendations and undertaken under similar ICP-OES operation conditions as used for the experimental fluid unknowns. The absolute % difference between the two measurements of Ca (6.55 ± 0.11 mg/L and 6.47 ± 0.12 mg/L; 1.2%), Mg (6.30 ± 0.09 mg/L and 6.25 ± 0.13 mg/L; 0.8%), and Si (0.15 ± 0.01 mg/L and 0.09 ± 0.01 mg/L; 50%) in ES-H-2 indicate adequate reproducibility of elements sufficiently above the detection limits (Ca: 0.005 mg/L; Mg: 0.01 mg/L; Si: 0.05 mg/L). The % bias for the mean of the two measurements relative to the certified standard concentrations provided by SCP Science (Ca: 6.50 mg/L; Mg: 6.11 mg/L) indicate excellent accuracy for Ca (0.15%) and Mg (2.7%); Si is not certified in ES-H-2 to allow for accuracy assessment.

Mineral precipitates

Precipitates collected using glass microfiber filters (GF/F) from the surface of reaction fluids were analyzed at the Department of Physics and Physical Oceanography at Memorial University of Newfoundland using a Bruker Alpha Fourier Transform Infrared (FTIR) spectrometer in an attenuated total reflectance (ATR) geometry with a broadband Globar (thermal) IR source and a diamond ATR crystal. Spectra recorded ATR intensity (absorbed light) as a function of wavenumber in the range of 400–4000 cm^{-1} at a resolution of 2 cm^{-1}.

Calculations

The CO_2 gas flux was calculated using measured CO_2 gas concentrations (Eq. 8) following the method described in Podgrajsek et al. (2013):

$$Flux = \frac{V(p_2 - p_1)}{RTA(t_2 - t_1)} \quad (8)$$

where V is the chamber volume (m^3), p_1 and p_2 are partial pressures (Pa) of gas measured at different points in time, R is the ideal gas constant (m^3 Pa K^{-1} mol^{-1}), T is the air temperature (K), A is the surface area of the fluid (m^2), and t_1 and t_2 are times the samples were taken (minutes). Eq. 8 assumes a linear change in CO_2 concentration with time. To measure the rate at which CO_2 is being removed from the chamber headspace, t_1 and t_2 must be measured before the gas and fluid have reached equilibrium as the flux results from

different concentrations between the fluid and gas, as well as their transfer velocity (Podgrajsek et al. 2013). Therefore, for this study, fluxes were reported for the first 30 min of the experiment where the change in CO_2 concentration was well described by a linear fit with an r^2 value > 0.97.

In experiments where it was likely that carbonates were formed, a carbon mass balance model was applied, which used CO_2 measurements from the chamber headspace and TIC measurements from the reaction fluids.

This model considered the reaction fluid in each experiment to be an aqueous system and that all CO_2 removed from the chamber headspace entered the aqueous phase. It was assumed that the change in CO_2 from the headspace ($\Delta[C]_{(g)}$) is accounted for by the change in aqueous inorganic carbon ($\Delta[C]_{(aq)}$) plus the amount of mineral precipitates ($\Delta[C]_{(s)}$) that formed (Eq. 9). By rearranging the equation, a carbon mass balance can predict the amount of carbonate minerals that precipitated in each experiment.

$$\Delta[C]_{(g)} = \Delta[C]_{(aq)} + \Delta[C]_{(s)} \quad (9)$$

Results

Mineralogy and petrography

XRD analysis of sub samples from crushed peridotite indicated that the dominant phases present in the rock were serpentine group minerals, olivine, brucite, carbonates, and talc (Fig. S1 in Supplementary Information). Thin sections were created from original rock samples used in experiments. All rock samples were highly serpentinized and had rusty orange weathered exterior surfaces; however, dark green surfaces were revealed when the oxidized exterior was removed. The following minerals were identified through microscopic observations: lizardite, olivine (forsterite), brucite, clinopyroxene, orthopyroxene (diopside), Cr-spinel, chrysotile, magnetite, and carbonate. Using SEM-MLA, the modal abundance of each mineral was determined. The following ranges were identified for the minerals, lizardite 83% to 87%, forsterite 7% to 10%, clinopyroxene 0% to 10%, brucite 0% to 5%, and cr-spinel 0% to 2%. All other minerals were less than 1% of thin section area (Table S1 in Supplementary Information). Brucite was present on the rim of primary minerals (olivine, pyroxene, and Cr-spinel) (Fig. 3A). The high degree of serpentinization created a pervasive mesh texture of lizardite, which replaced 80% to 100% of the original minerals (Figs. 3B and 3D). Cross-cutting fractures were filled with chrysotile, brucite, magnesite, and carbonate (Fig. 3C).

CO_2 sequestration

All experiments showed decreases in gaseous CO_2 headspace concentration over time, except for the baseline experiment with only deionized water (Fig. 4). Control trials investigating waters in the absence of crushed ultramafic rock found that deionized water had no measurable change in headspace CO_2 concentrations outside of standard deviation while ultra-basic waters had the greatest CO_2 flux of 323 ppm (± 4 ppm, 1σ, $n = 3$), which was more than double that of basic waters without rock at 128 ppm (± 2 ppm, 1σ, $n = 3$), (two sample t test, $p = 1.7 \times 10^{-5}$).

In the presence of crushed ultramafic rock, all water types sequestered CO_2. Similar to waters in the absence of crushed ultramafic rock, the ultra-basic waters with crushed ultramafic rock sequestered the most CO_2 of all three water types with a CO_2 decrease of 225 ppm (± 9 ppm, 1σ, $n = 3$). In the presence of crushed ultramafic rock, deionized water sequestered 70 ppm (± 9 ppm, 1σ, $n = 3$), which was not significantly different from the amount of CO_2 sequestered by basic waters in the presence of crushed ultramafic rock at 85 ppm (± 6 ppm, 1σ, $n = 3$) (two sample t test, $p = 7.7 \times 10^{-2}$). In the presence of ultramafic rock, deionized waters had a measurable decrease in headspace CO_2 concentration, which was not observed by deionized water alone. Basic and ultra-basic waters containing crushed ultramafic rock also sequestered CO_2; however, the amount of CO_2 sequestered was significantly lower than their counterparts that did not contain rock (two sample t test, $p = 3.2 \times 10^{-3}$, $p = 4.8 \times 10^{-4}$) (Fig. 5A).

CO_2 flux

During the first 30 min, the relationship between CO_2 concentration and time was linear (i.e., $r^2 \geq 0.98$). All experiments (with the exception of deionized water) had a measurable negative CO_2 flux, which indicated that CO_2 was being removed from the gaseous headspace at the air–water interface. (Fig. 5B). When crushed rock was added to deionized water, the CO_2 flux was -2.5×10^{-4} mol/m^{2}min ($\pm 9 \times 10^{-5}$ mol/m^{2}min, 1σ, $n = 3$) (Fig. 5B). Deionized water with crushed rock showed no significant difference in flux values when compared with flux values of basic water experiments with and without crushed rock (ANOVA single factor, $p = 1.5 \times 10^{-1}$). Ultra-basic water had the largest negative CO_2 flux out of all experiments at 1.40×10^{-3} mol/m^{2}min ($\pm 3 \times 10^{-5}$ mol/m^{2}min, 1σ, $n = 3$). Adding crushed rock to ultra-basic water significantly reduced the negative flux to 1.06×10^{-3} mol/m^{2}min ($\pm 7 \times 10^{-5}$ mol/m^{2}min, 1σ, $n = 3$) (two sample t test, $p = 6.9 \times 10^{-3}$).

Aqueous measurements

All experiments showed an increase in aqueous TIC except for deionized water experiments whose TIC remained below the detection limit. Experiments performed with crushed rock had much larger increases in TIC compared to experiments performed without rock but also had poorer precision (Fig. 6F). The largest increase in TIC was observed in basic with rock experiments that had an increase of 5.07×10^4 mol ($\pm 3.28 \times 10^4$ mol, 1σ, $n = 3$).

The largest changes in pH were observed in experiments that had crushed rock added to them. When crushed rock was added to deionized water, the pH increased from 6.04 (± 0.35, 1σ, $n = 3$) to 10.02 (± 0.12, 1σ, $n = 3$) for a change of 3.96 (± 0.28, 1σ, $n = 3$) (Figs. 6A and 7). Conversely, when crushed rock was added to ultra-basic waters the pH decreased from 12.05 (± 0.04, 1σ, $n = 3$) to 10.57 (± 0.11, 1σ, $n = 3$) for a change of -1.48 (± 0.07, 1σ, $n = 3$). Basic and ultra-basic experiments without crushed rock had minor pH decreases of

Fig. 3. Thin section photomicrograph (A-C) and scanning electron microscope backscattered electron (SEM-BSE) image (D) of Blow Me Down ultramafic peridotite. (A) brucite (brc) on the rim of cr-spinel (spl) grain in a matrix of fine-grained lizardite (lz) with remnant olivine (ol) grains and magnetite (mt). (B) mesh-textured lizardite (lz) that has replaced olivine (ol) grain. (C) Chrysotile (ctl) vein flanked by carbonate (crb) on both sides and brucite (brc) in a matrix of lizardite. (D) SEM image showing mesh texture of lizardite (lz) with vein of carbonate (crb) cross-cutting the field of view.

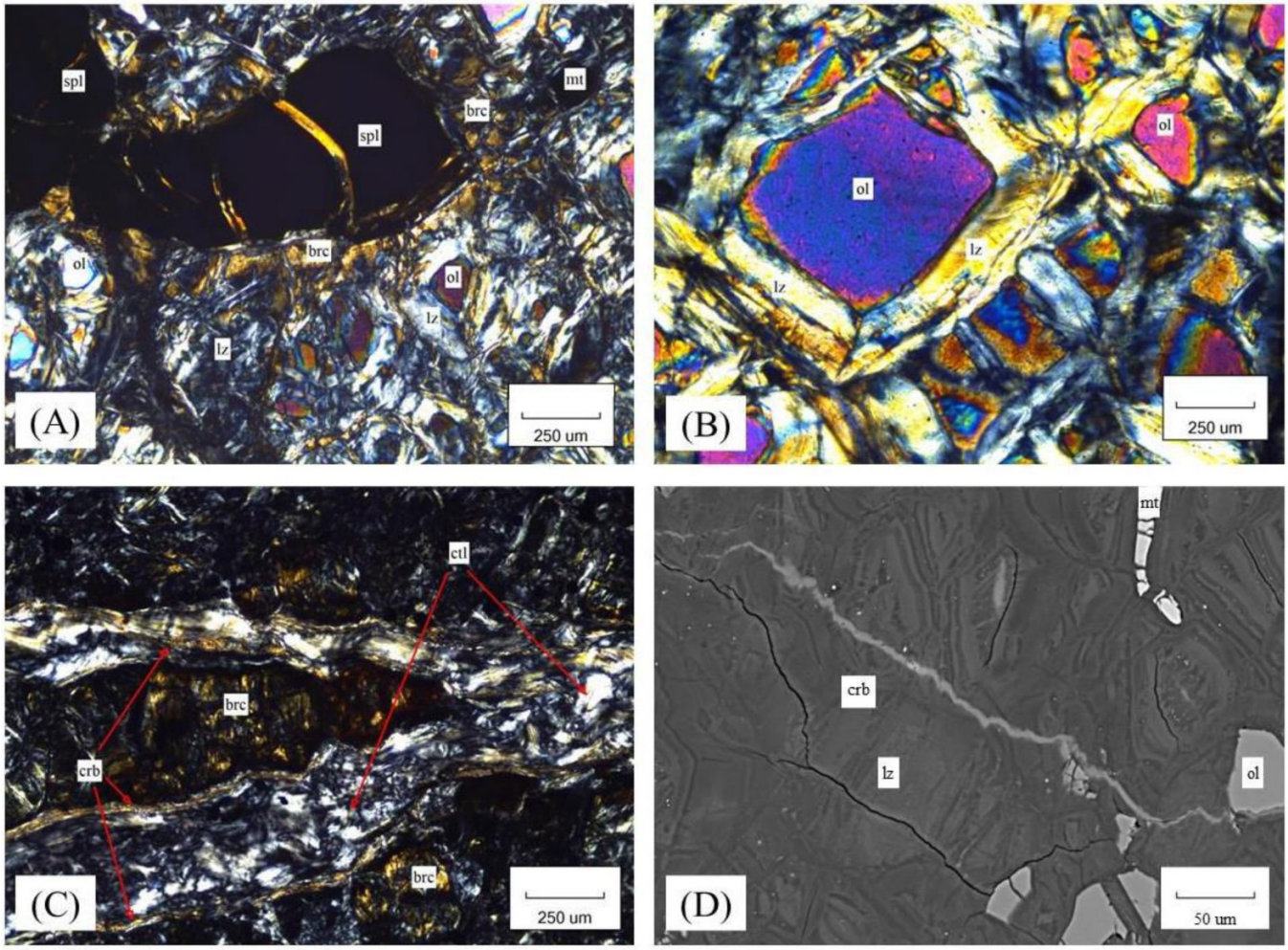

0.69 (±0.04, 1σ, n = 2) and 0.17 (±0.04, 1σ, n = 3), respectively. pH changes in all other experiments were less than reproducibility.

The conductivity of the fluids was measured before and directly after each experiment. All experiments except for deionized water without crushed rock had measurable changes in conductivity. Ultra-basic experiments with rock had the greatest decrease in conductivity of 555.3 μs/cm (±64.9 μs/cm, 1σ, n = 3) (Fig. 6B). Without crushed rock, ultra-basic waters had a significantly smaller decrease in conductivity of 203.9 μs/cm (±20.2 μs/cm, 1σ, n = 3) (Fig. 6B). Basic water experiments had a significantly smaller decrease in conductivity of 13.80 μs/cm (±10.13 μs/cm, 1σ, n = 3) (two sample t test, $p = 8.7 \times 10^{-4}$) (Fig. 6B). Deionized water without rock had no measurable change in conductivity. Deionized water and basic water experiments both had similar increases in conductivity when crushed rock was added to them. They increased by 106.6 μs/cm (±19.0 μs/cm, 1σ, n = 3) and 105.5 μs/cm (±33.9 μs/cm, 1σ, n = 3), respectively (Fig. 6B). The largest change in conductivity was a decrease in ultra-basic waters with rock of 555.3 μs/cm (±64.9 μs/cm, 1σ, n = 3) (Fig. 6B).

Reaction kinetics

Subsequent experiments were performed on pH endmember fluids (i.e., deionized water and ultra-basic water) in the presence of ultramafic rock to measure the kinetic relationships of both conductivity and pH. Ultra-basic waters in the presence of ultramafic rock showed a decrease in CO_2 concentration over 4 h and had an exponential relationship (R^2 = 0.93). The pH of ultra-basic waters in the presence of ultramafic rock showed a steady decrease overtime linearly (r^2 = 0.99) (Fig. 8A). However, conductivity did not have a linear or exponential relationship (i.e., r^2 and R^2 < 0.90) as it showed an initial rapid decrease which tapered off over

Fig. 4. Average CO_2 concentrations (ppm) measured during triplicate 240 min (4 h) CO_2 sequestration experiments varying water chemistry (deionized water, basic water, and ultra-basic water) with (orange) and without (blue) crushed rock. Confidence bands represent standard deviation ($\pm 1\sigma$) from triplicate measurements for the duration of the experiment.

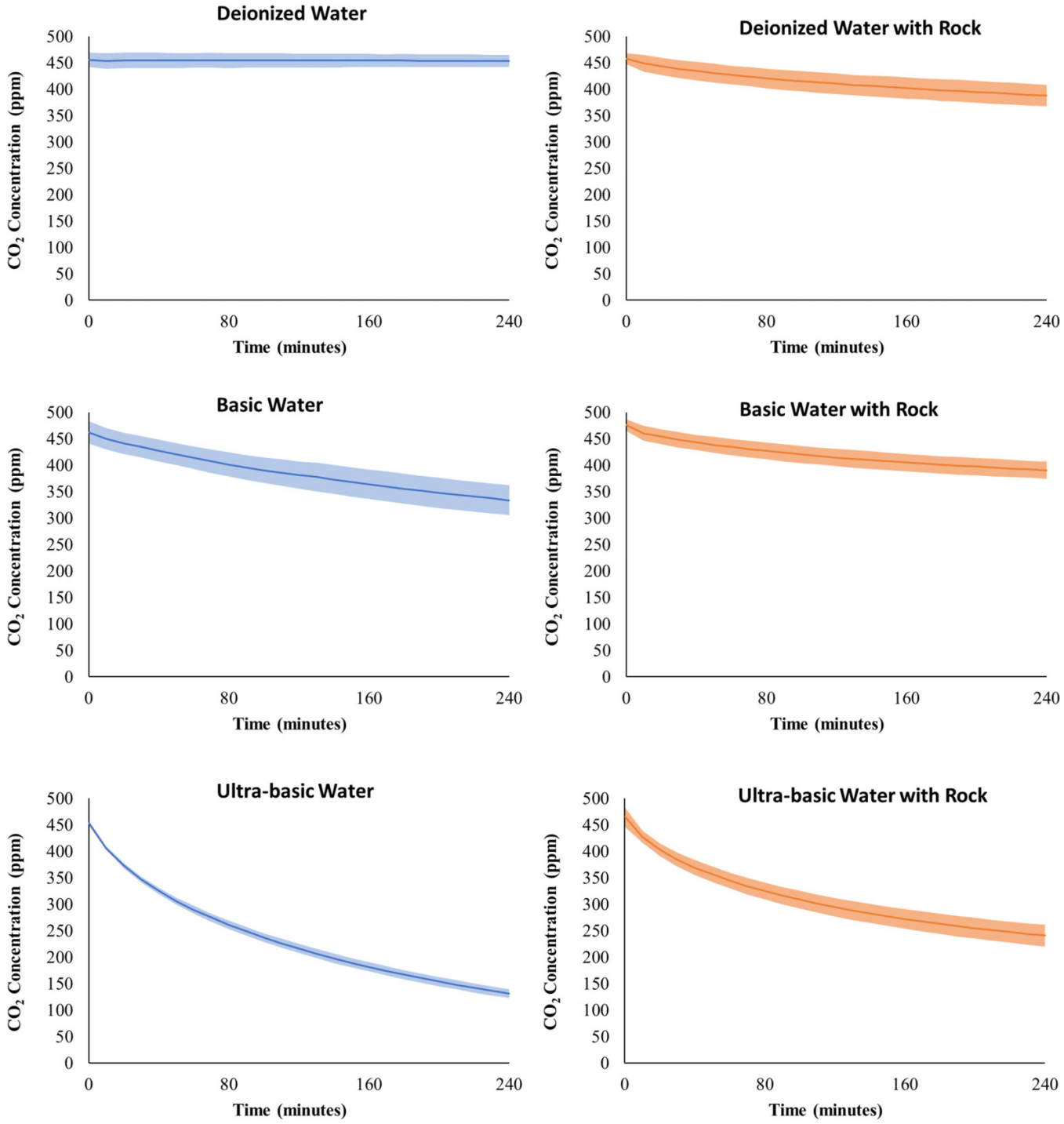

time (Fig. 8B). The decrease in CO_2 concentration of deionized water with rock experiments had an exponential relationship ($R^2 = 0.97$). However, the change in pH of deionized water with rock experiments showed an initial large increase in the first 15 min from 6.28 ± (0.22, 1σ, $n = 3$) to 9.63 ± (0.18, 1σ, $n = 3$), after which there was little to no change (Fig. 8A). The conductivity of the deionized water with rock experiment did not have a linear or exponential relationship (i.e., r^2 and $R^2 < 0.90$) as it rapidly increased between 0 and 15 min from 6.28 ± (0.22, 1σ, $n = 3$) to 9.63 ± (0.18, 1σ, $n = 3$); after 15 min, the pH showed little change (Fig. 8A).

Fig. 5. (A) Average change in CO_2 concentration measured from triplicate experiments varying water chemistry (deionized water, basic water, and ultra-basic water) with and without crushed ultramafic rock. The change was calculated by subtracting initial CO_2 concentrations from final CO_2 concentrations. Error bars represent standard deviation ($\pm 1\sigma$) of the average change in CO_2 concentration. (B) Average CO_2 flux values calculated from triplicate experiments varying water chemistry (deionized water, basic water, or ultra-basic water) with and without the addition of crushed rock. The flux was calculated using data collected during the first 30 min of each experiment when the relationship between CO_2 concentration and time was linear. Error bars represent standard deviation ($\pm 1\sigma$) of the average CO_2 flux. Stars represent significance level, *, p value ≤ 0.05, **, p value < 0.01, ***, p value < 0.001, ****, and p value < 0.0001. Significance level was determined using heteroscedastic t-tests comparing each value to blank baseline experiments using deionized water only.

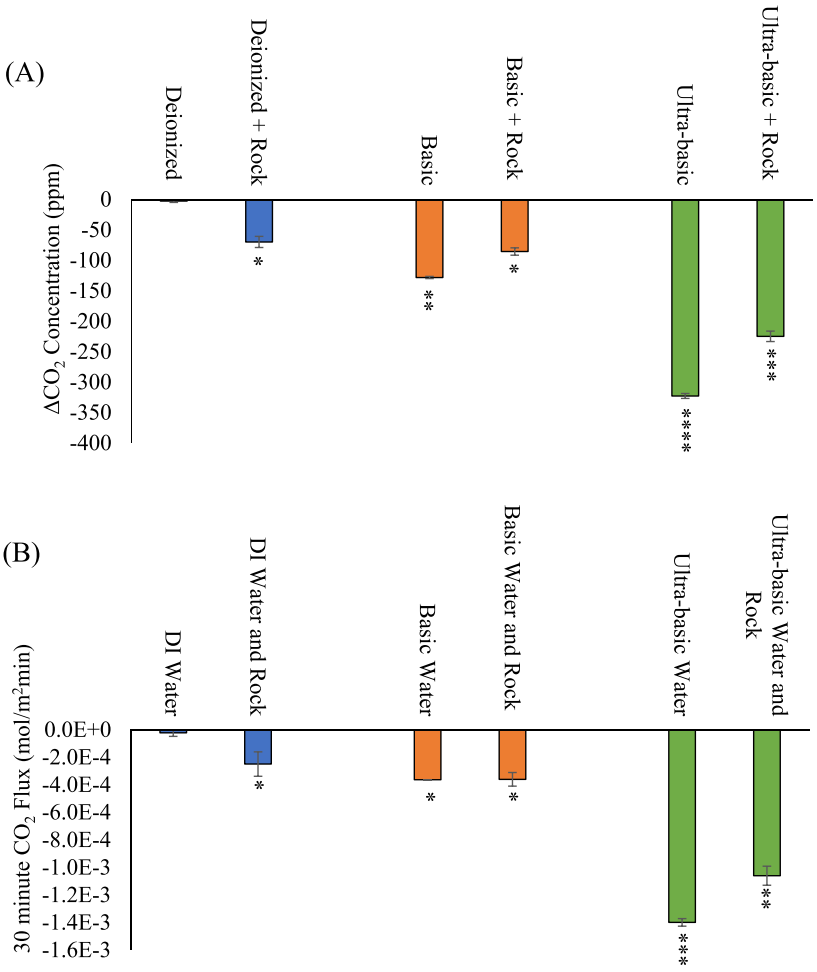

Ion concentrations

The change in Ca, Mg, Si, and TIC concentrations in the fluids were monitored by sampling the fluid before and directly after each experiment. All experiments using crushed rock had greater changes in ion concentrations compared to experiments without rock (Figs. 6C, 6D, and 6E). Ultra-basic water with crushed rock experiments had the largest decrease in Ca of 1.01×10^{-3} mol/L ($\pm 8 \times 10^{-5}$ mol/L, 1σ, $n = 3$). Without the addition of crushed rock, ultra-basic experiments had a significantly smaller decrease in Ca of 3.57×10^{-4} mol/L ($\pm 5.4 \times 10^{-5}$ mol/L, 1σ, $n = 3$) (two sample t test, $p = 5.2 \times 10^{-4}$) (Fig. 6C). All experiments using crushed rock had an increase in Mg concentration; basic water with rock experiments had the greatest increase of 8.21×10^{-4} mol/L ($\pm 2.71 \times 10^{-4}$ mol/L, 1σ, $n = 3$) (Fig. 6D). No change in Mg concentration was observed in experiments without rock. All experiments using crushed rock had small increases in Si concentration significantly greater than experiments that did not have crushed rock (ANOVA single factor, $p = 6.3 \times 10^{-6}$) (Fig. 6E).

Infrared spectroscopy

Ultra-basic experiments both in the presence and absence of crushed ultramafic rock had a white film of mineral precipitates visible on the surface immediately after the 4 h observations (Fig. 9). The precipitates were collected from the water surface using a glass microfiber filter and analyzed using FTIR. A blank glass microfiber filter was measured as a baseline (Fig. 10A) and subsequently the precipitates collected from ultra-basic waters with crushed ultramafic rock and without crushed ultramafic rock. Both ultra-basic waters in the presence and absence of crushed ultramafic rocks showed distinctive wavelengths at 875 cm^{-1} and 1400 cm^{-1} (Figs. 10B

Fig. 6. The average change in pH, conductivity, ion concentrations (Ca, Mg, and Si), and total inorganic carbon (TIC) measured during 4 h (240 min) CO_2 sequestration experiments varying water chemistry (deionized water, basic water, or ultra-basic water) with and without the addition of crushed peridotite rock. All changes were calculated by subtracting initial measurements from final measurements. Error bars represent standard deviations ($\pm 1\sigma$) calculated from triplicate experimental trials.

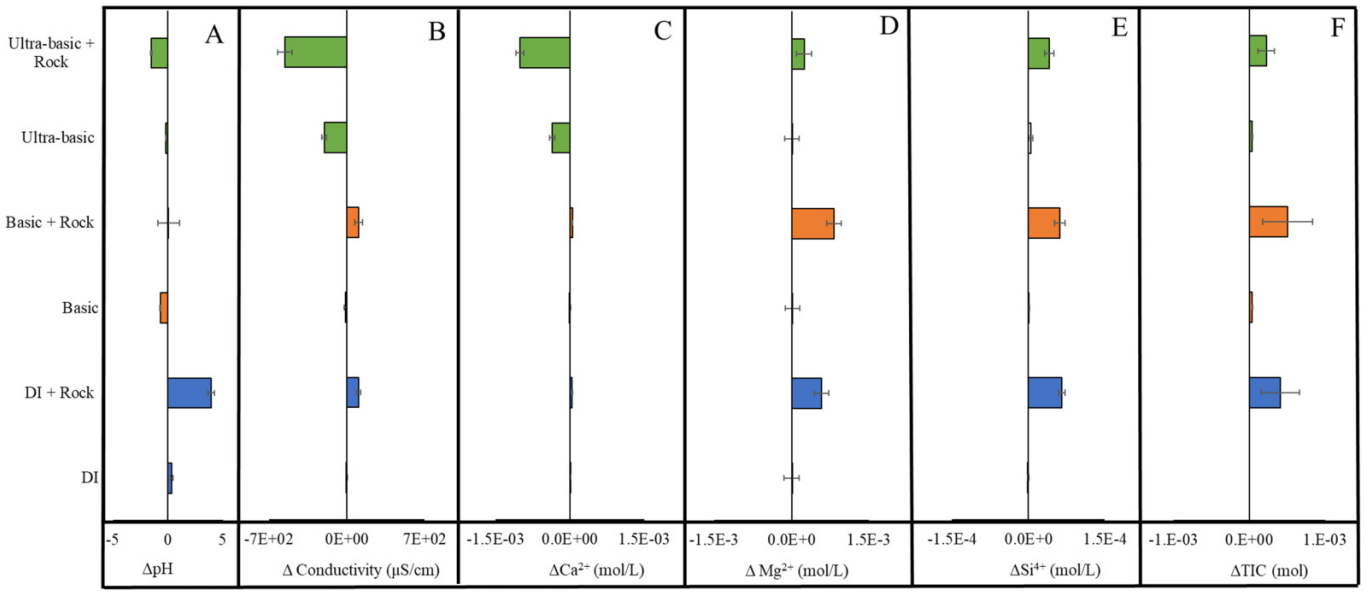

Fig. 7. Average pH values measured before and after each 4 h (240 min) CO_2 sequestration experiment. The experiments were run in triplicate and varied water chemistry (deionized water, basic water, or ultra-basic water) with and without the addition of crushed rock. The initial (I) pH measured at 0 min and final (F) pH measured at 240 min. Error bars represent standard deviation ($\pm 1\sigma$) determined from triplicate experiments.

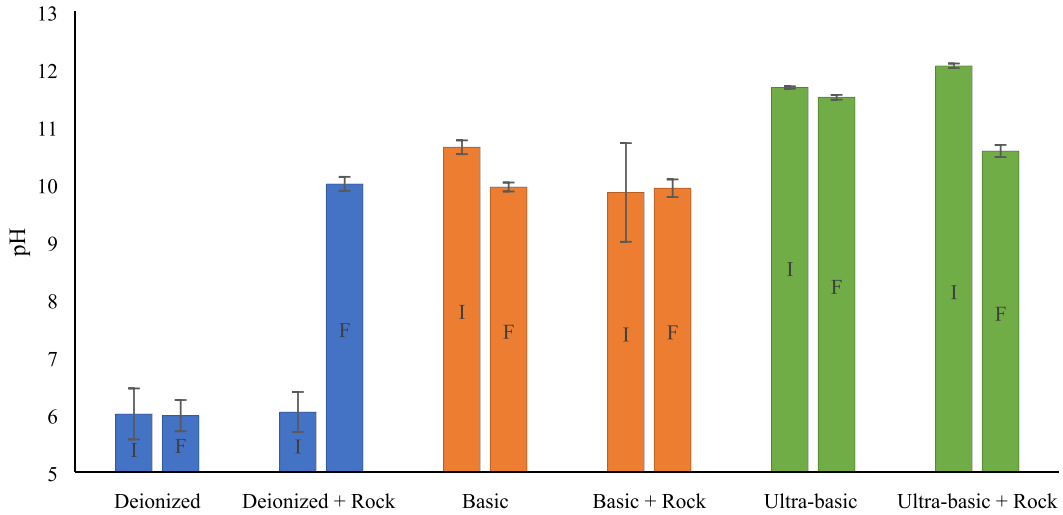

and 10C, respectively). These spectral peaks were consistent with spectral peaks associated with calcite (Fig. 10D).

Discussion

CO_2 sequestration as a function of pH and mineral dissolution

The aqueous chemistry of the experimental water alone had an affect on the amount of CO_2 sequestered and CO_2 flux. Deionized water (pH ~7) was used as a baseline while basic waters (pH ~10) and ultra-basic waters (pH ~12) were used to simulate naturally occurring Type I and Type II peridotite-hosted groundwaters found in ophiolite terrains. Without the addition of ultramafic rock, ultra-basic and basic waters sequestered CO_2, with the former having a significantly higher CO_2 flux (two sample t test, $p = 1.7 \times 10^{-5}$). Deionized water alone had no measurable CO_2 flux outside standard deviation. In control experiments, the sequestration of CO_2 was driven by the pH of the solution and neutralization

Fig. 8. (A) Average conductivity measurements (μS/cm) taken over time during 4 h experiments for ultra-basic with rock experiments (UB + Rock) and deionized water with rock experiments (DI + Rock). Error bars represent standard deviation ($\pm 1\sigma$) from triplicate measurements. (B) Average pH measurements taken during 4 h experiments for ultra-basic and deionized water with rock experiments. Error bars represent standard deviation ($\pm 1\sigma$) from triplicate experiments.

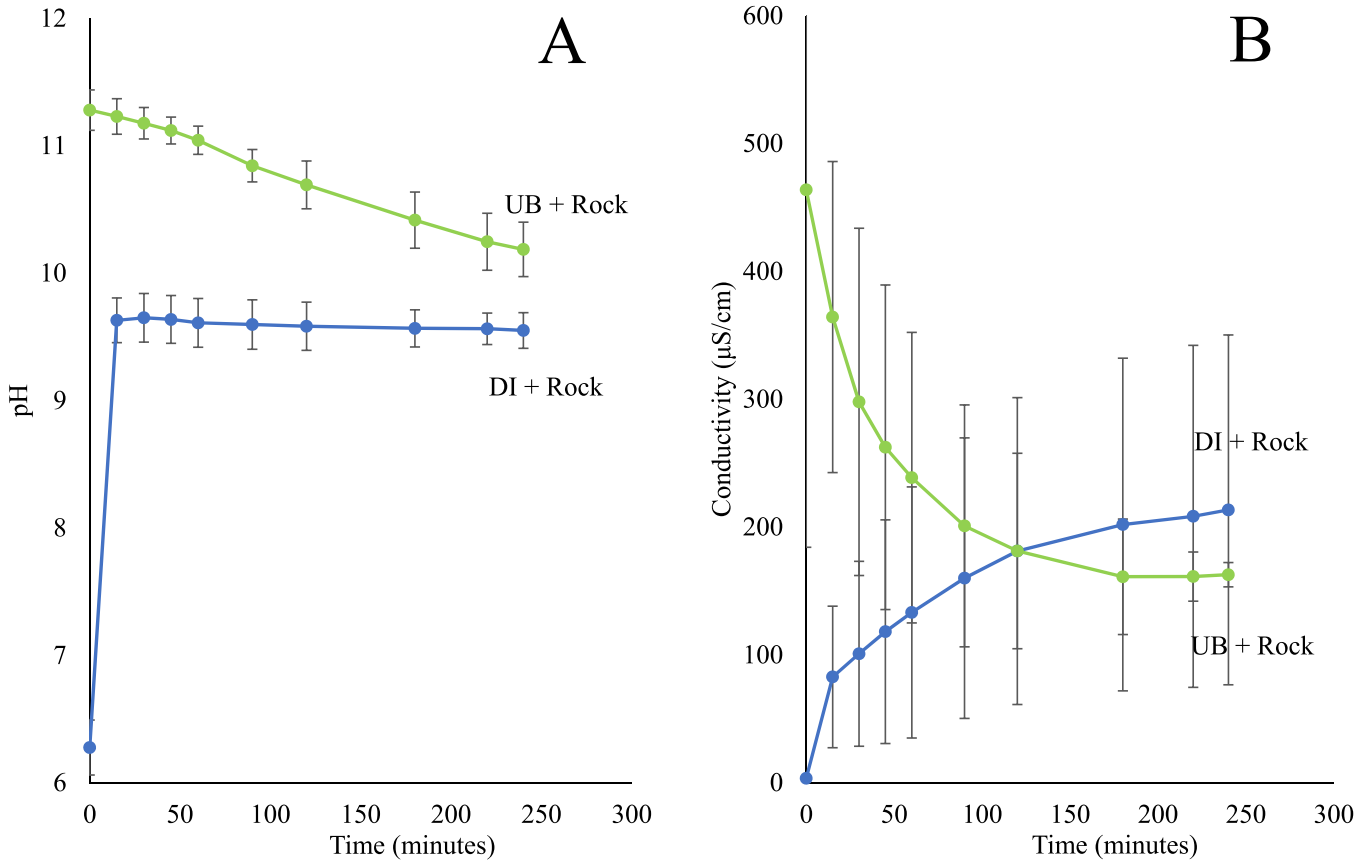

Fig. 9. Photographs of white films on calcium hydroxide rich waters after the 4 h ultra-basic carbon sequestration experiments. (A) Without the addition of crushed peridotite and (B) with the addition of crushed peridotite.

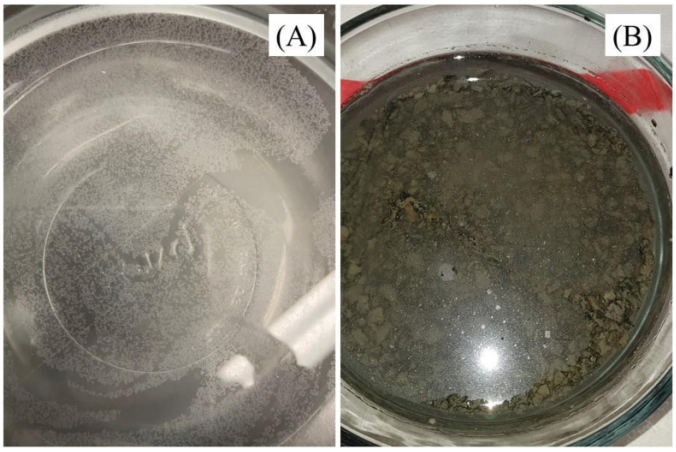

reactions (i.e., acid–base equilibria) (Table S2 in Supplementary Information). Hence, the higher the pH, the faster CO_2 was sequestered. Therefore, in natural systems, Type II waters likely sequester CO_2 faster than Type I waters.

In deionized water experiments, the starting pH was 6.04 (± 0.34, 1σ, $n = 3$) and the addition of crushed ultramafic rock caused an increase in the pH and therefore a greater reduction in headspace CO_2 concentration. In contrast, the starting pH of ultra-basic waters was 12.05 (± 0.04, 1σ, $n = 3$) and the addition of crushed ultramafic rock reduced the fluids pH resulting in less CO_2 being sequestered compared to the ultra-basic water control trials. In basic water experiments, the initial fluid pH was already close to the equilibrium pH and, within the 4 h experiment, remained unchanged within standard deviation. It is likely that the reduced CO_2 sequestration in basic water experiments in the presence of ultramafic rock was due to an increase in ionic strength via rock dissolution (Table S3 in Supplementary Information). As ionic strength increases, a solution's ability to sequester CO_2 is reduced. The effect of ionic strength on CO_2 headspace concentrations was not observed in deionized waters or ultra-basic waters as the change in pH resulting from rock dissolution had a much greater effect on CO_2 sequestration.

In experiments presented here, the selected grain size was less than 0.7 cm; finer particles present in the crushed rock would increase the overall sample surface area and could attribute to more rapid dissolution rates and changes in ionic strength. Of all minerals identified in the ultramafic samples, the mineral brucite was identified as the most soluble phase

Fig. 10. FTIR spectrum for precipitates collected from ultra-basic waters with and without the addition of crushed peridotite. The top spectrum was taken from a blank glass microfiber filter without any precipitate collected on it. The middle two spectra are from a glass microfiber filter that was used to collect precipitate from ultra-basic experiments with and without rock. The bottom spectrum was taken from a known calcite reference standard.

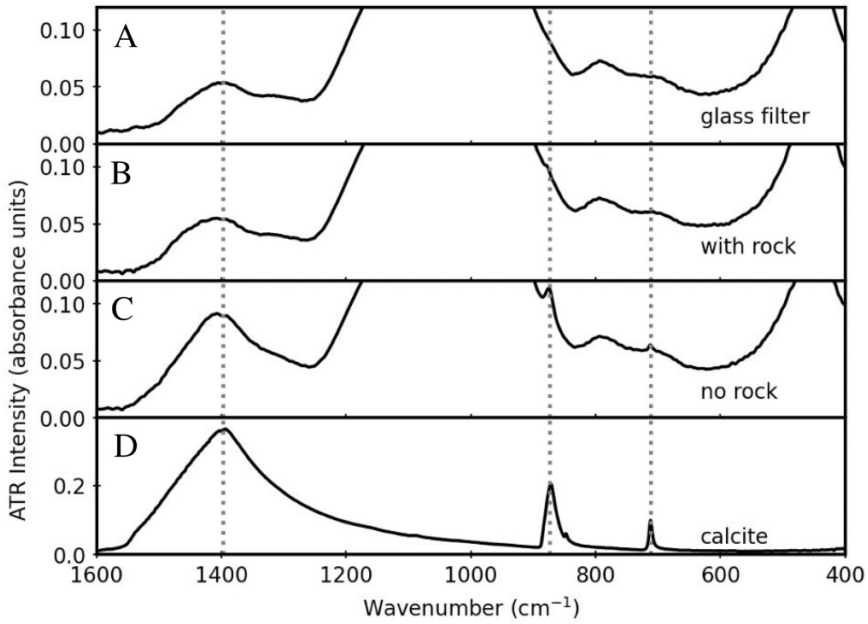

in the rocks. At standard conditions, brucite has a K_{sp} of 1.8 x 10^{-11} and an equilibrium pH of 10.37 (Pokrovsky and Schott 2004). In the experiments with crushed peridotite, the pH values were near to, or approaching, this equilibrium pH. However, it was unknown when these values were reached. More detailed time series experiments revealed that the deionized water with rock experiments approached this equilibrium pH within 15 mins, likely due to a near-neutral starting pH and low ionic strength, which favoured the rapid dissolution of ultramafic minerals such as brucite. The ultra-basic with rock experiment also approached this equilibrium pH value, but gradually over the 4 h period. Although beyond the scope of this study, longer experimental trials would allow for the determination of the equilibrium constant associated with this peridotite, as well as peridotites of different mineralogy.

In addition to changes in pH, there was other evidence that peridotite was dissolving in the experiments. In deionized water and basic water experiments with crushed rock, there were increases in conductivity, ionic strength, and aqueous Mg, Ca, and Si (Figs. 6C, 6D, and 6E). Dissolution of peridotite was also likely present in ultra-basic experiments as there was a measurable increase in Mg (Fig. 6D). However, in ultra-basic waters in the presence of ultramafic rock, a decrease in conductivity, Ca concentration, and ionic strength indicated that mineral precipitation was more likely the dominant process compared to mineral dissolution in these experiments.

Precipitation of carbonates

In ultra-basic waters both in the presence and absence of crushed ultramafic rock, CO_2 was converted to solid Ca carbonates. The first indication of this precipitation was the observed decrease in conductivity and aqueous Ca concentration. Additionally, the thin white film that formed on the surface of the water in both experiments (Fig. 9) was measured using FTIR. Spectral peaks consistent with calcite were present at 875 cm^{-1} and 1400 cm^{-1} in both ultra-basic experiments with and without rock (Figs. 10B and 10C).

Using a carbon mass balance model (Equation 9), it was estimated that ultra-basic without rock experiments precipitated 6.33×10^{-5} moles ($\pm 9.8 \times 10^{-6}$ mole, 1σ, $n = 3$) of carbonate. This indicates that roughly 59% of the 1.01×10^{-4} moles ($\pm 2 \times 10^{-6}$ moles, 1σ, $n = 3$) of CO_2 removed from the chamber headspace was converted to solid carbonate (Fig. 11). In experiments using crushed rock, it is likely that CO_2 from the chamber headspace was not the only source of aqueous carbon. Experiments using crushed rock showed a greater increase in the moles of TIC in the water compared to moles of C removed from the chamber headspace (Fig. 11). Since the experiments were performed in a closed system, it is likely that the increase in TIC for experiments using crushed rock was caused by the dissolution of carbonates initially present (Table S1 in Supplementary Information) in the crushed peridotite. Although typically carbonates are buffered from dissolving in high pH waters, the waters used in these experiments were sparged with nitrogen to remove dissolved CO_2 prior to the experiment. This caused the waters to be undersaturated in carbonate ions allowing for the dissolution of solid carbonates present in the ultramafic rock (Anderson 2013). In ultra-basic with rock experiments, at the start of the experiment carbonates within the ultramafic rock dissolved. Once the carbonate ion concentration in the water increased, solid carbonates began to precipitate. The precipitation of Ca carbonates in ultra-basic water with rock experiments is

Fig. 11. Average change of moles of C leaving the chamber headspace and average change in moles of TIC in the reaction fluid for each experimental trial. Changes were calculated by subtracting initial value from final value and were reported as absolute values for comparison. Error bars represent standard deviation from triplicate experiments.

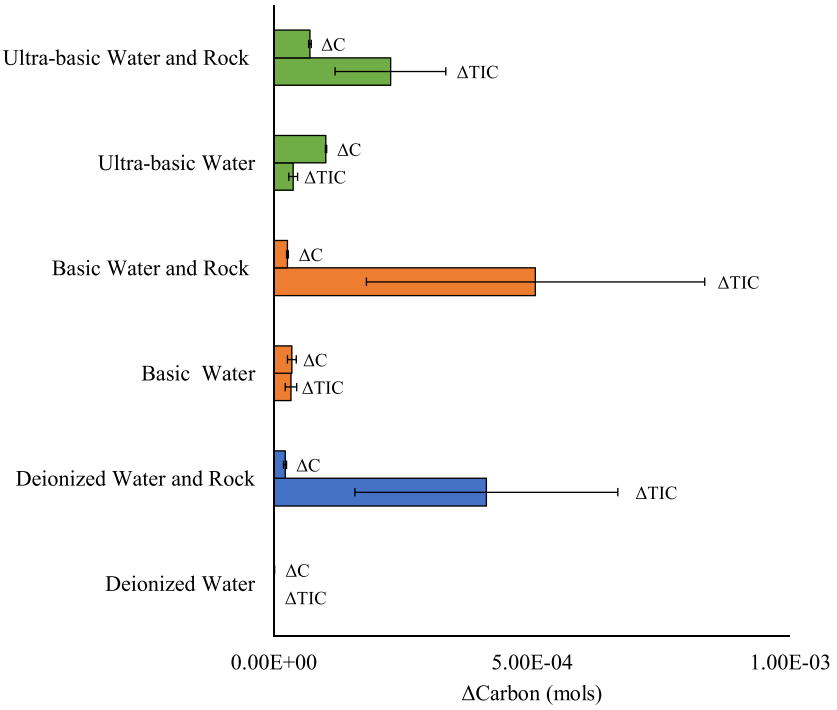

supported by a decrease in Ca concentration (Fig. 6C) coupled with a white precipitate on the surface (Fig. 9), which had FTIR spectral peaks at 875 cm^{-1} and 712 cm^{-1} consistent with calcite (Fig. 10). In a real-world application of surficial CDR, the circulating fluids would be constantly saturated with carbonate ions, while solid carbonates would be removed from the system as they precipitated within fractures of the peridotite.

Although all experiments performed in the presence of ultramafic rock had increases in magnesium activity, the precipitation of magnesium carbonates was not detected in any trials (Table S3 in Supplementary Information). Unlike calcite which precipitates at low temperatures, the precipitation of magnesite is kinetically inhibited at ambient conditions due to the slow desolvation rate of water from magnesium (Saldi et al. 2009). Additionally, magnesite has a K_{sp} of 1.0×10^{-5}, indicating it is much more soluble than other carbonates such as calcite with a K_{sp} of 3.8×10^{-9}.

Ultra-basic waters as a proxy for Type II springs

In both control experiments and experiments that contained crushed rock, the rate at which CO_2 was being sequestered appeared to slow over time (Fig. 4). Graphical plots were used to determine if a reaction was first order or second order. It was apparent that all CO_2-consuming reactions could be well described by a first-order or second-order relationship with the second-order reactions having a slightly better fit (Table S4 in Supplementary Information). This indicated that the reactions could be rate dependent on either the consumption of CO_2 alone (i.e., first order) or by the consumption of CO_2 and an additional reactant in the water such as hydroxide (i.e., second order).

The pH and ion concentrations of synthetic ultra-basic groundwaters from this study had comparable pH values and Ca and Mg concentrations to Type II waters sampled at sites of serpentinization in California by Barnes et al. (1967), in Oman by Giampouras et al. (2020), and in Newfoundland by Cook et al. (2021) and Szponar et al. (2013) (Table 1). The interaction of meteoric waters with peridotite in the subsurface generates Type I and subsequently Type II groundwaters. The mineralogy of the ferromagnesian minerals is reflected in the chemistry of these water types. Lithostatic pressure can cause these waters to return to the surface and produce Type I and Type II springs. The CO_2 flux of one of these Type II ultra-basic springs in the BOIC was measured by Morrissey and Morrill (2017) using a closed floating chamber. The results of this field experiment were compared to the results of ultra-basic laboratory experiments to determine if they provided a good proxy for CO_2 fluxes occurring in natural ophiolite systems. In the field experiment conducted by Morrissey and Morrill (2017) in the Tablelands, an average flux of 1.9×10^{-5} mol/m^2min was calculated from the 226 min observation. In this experiment, the relationship between CO_2 concentration and time was linear ($r^2 = 0.91$). Similarly, ultra-basic water with crushed rock experiments performed in this study had an average 240 min flux of 1.83×10^{-5} mol/m^2min ($\pm 7 \times 10^{-7}$ mol/m^2min, 1σ, $n = 3$). In this experiment, the relationship between CO_2 concentration and time was also linear ($r^2 = 0.92$). This demonstrates that experiments performed in this study realistically simulated carbon

Table 1. pH, calcium concentration, and magnesium concentration measured in synthetic basic and ultra-basic groundwaters, as well as natural Type I and Type II spring locations found at sites of serpentinization.

Water Type	Location	Reference	pH	Ca (mol/L)	Mg (mol/L)
Type I	Oman	Giampouras et al. (2020)	8.2 to 9.4	1.8E−4 to 4.3E−4	1.4E−3 to 7.2E−3
	California	Barnes et al. (1969)	7.8 to 9.0	7.2E−5 to 3.5E−4	1.7E−3 to 1.1E−2
	Newfoundland	Cook et al. (2021)/Szponar et al. 2013	N/A	N/A	N/A
	Synthetic Groundwater	This study	9.8 to 10.3	1.4E−6 to 2.7E−6	1.0E−4 to 1.4E−4
Type II	Oman	Giampouras et al. 2020	11.6 to 12.2	1.6E−3 to 2.0E−3	1.0E−6 to 1.7E−5
	California	Barnes et al. (1969)	11.25 to 12.01	8.7E−4 to 1.3E−3	2.5E−6 to 1.7E−5
	Newfoundland	Cook et al. 2021/Szponar et al. 2013	10.1 to 13.1	8.1E−4 to 1.5E−3	1.2E−15 to 6.3E−5
	Synthetic Groundwater	This study	12.01 to 12.09	1.1E−3 to 1.3E−3	1.7E−6 to 2.1E−6

sequestration occurring at natural ultra-basic springs. To our knowledge, similar measurements have not been performed on Type I basic spring sites.

Carbon sequestration potential

Kelemen et al. (2020) estimated the total carbon mineralization potential of the Semail Ophiolite of Oman based on complete carbonation of the ultramafic rock. According to this study one tonne of olivine can convert 0.51 metric tonnes of CO_2 to carbonate minerals, 1 tonne of brucite can convert 0.63 metric tonnes of CO_2 to carbonate minerals, and 1 tonne serpentine or pyroxene minerals can convert 0.41 tonnes of CO_2 to carbonate minerals (Kelemen et al. 2020). We applied these conversion rates to our study. Using QGIS, a total surface area for the BOIC ultramafic rocks was determined to be 408 km^2; at an estimated depth of 1 km (Girardeau and Nicolas 1981), this gives a total volume of ultramafic rock of 408 km^3. Using a calculated density of 3.08 g/cm^3, the BOIC comprises 1.3×10^{12} tonnes of rock. Applying the lower estimate for CO_2 conversion of 0.41 metric tonnes of CO_2 per tonne of ultramafic rock gives a total CO_2 storage capacity of 5.1×10^{11} tonnes for the entire BOIC. This estimate is over 700 times greater than the average 670 megatonnes of annual CO_2 emissions for all of Canada (Government of Canada 2021). While this estimate considers complete carbonation of the BOIC, which is realistically not possible, even a 1% carbonation of the ophiolite could account for >7 years of Canadian CO_2 emissions.

Kelemen and Matter (2008) provided an estimate for the total carbon mineralization potential of the Semail Ophiolite based on dissolved inorganic carbon content of Type I waters. Their calculation assumes that all dissolved inorganic carbon in Type I basic waters is consumed to form magnesite in the subsurface. It was determined that every km^3 of ultramafic rock in the Semail Ophiolite naturally consumes 2 tonnes of CO_2 annually via this process. In this study, the addition of 300 g of ultramafic rock to 300 mL deionized water sequestered 2.17×10^{-5} moles ($\pm 2.8 \times 10^{-6}$ moles, 1σ, $n = 3$) of CO_2. If the amount of CO_2 sequestered for 300 g of rock is upscaled to 1 km^3, than 9.9×10^3 tonnes of CO_2 would be sequestered. If this result is then applied for the entire volume of the BOIC, over 4 million tonnes of atmospheric CO_2 could be sequestered. While laboratory experiments here used rocks with a much greater reactive surface area, it is likely that in a natural system increasing the reaction time could allow for similar results. In natural systems, the process of reactive cracking (Rudge et al. 2010) is also possible. In this process, the increase in volume associated with carbonate precipitation causes ultramafic rock to fracture along planes of weakness. As fractures propagate, fresh ultramafic rock becomes exposed, which can then be dissolved by water creating a positive feedback loop.

Significance

This study demonstrates that carbon mineralization of the ultramafic rocks within the BOIC has the potential to remove a significant quantity of atmospheric CO_2. It is estimated that global CO_2 emissions in 2022 were approximately 36.8 Gt (IEA 2022). Applying the conversion factor from Kelemen et al. (2020) it is estimated that complete carbonation of the BOIC ultramafic rocks would consume 510 Gt of atmospheric CO_2, which would constitute over 13 years of global CO_2 emissions. In this study, it is shown that the ultramafic rock in the presence of water sequestered CO_2 and has the potential to form basic and ultra-basic waters that sequester atmospheric carbon. Forming carbonates is a key step in long-term storage of CO_2 and preventing CO_2 from re-entering the atmosphere. In experiments presented here, the addition of crushed peridotite to deionized water rapidly generated a high pH water capable of sequestering CO_2. As observed, the dissolution of rock, which causes CO_2 sequestration, is kinetically favourable even at ambient conditions. By injecting CO_2-enriched waters into the subsurface, this process could likely be industrialized and require little energy input beyond drilling and pumping waters into the subsurface. Additionally, the increased pressure and temperature at depth would trigger the precipitation of magnesite allowing for carbon to be stored in a solid form. The employment of ultramafic rocks for CO_2 storage could significantly contribute the Canada's net zero emissions target by the year 2050.

Acknowledgements

This study was supported in part by grants from Natural Sciences and Engineering Research Council (NSERC) Discovery

Grant and Collaborative Research and Development, as well as matching and in-kind support from Newfoundland and Labrador's Energy Corporation (Nalcor) awarded to PLM. The authors would like to thank Mark Wilson for his help in the field and many inspirational discussions, Timilehin Oguntuyaki for his assistance in the field, Ben Taylor for his assistance and guidance with laboratory work, Steve Emberley for his guidance and thoughtful discussions, the Biogeochemistry of Boreal Ecosystems Research Group (BBERG), specifically Jenika Marshall for her assistance with TIC samples, and Memorial University's CREAIT Network for their support, specifically: Dylan Goudie (CREAIT—Microanalysis Facility), Dr. Markus Wälle (CREAIT—Microanalysis Facility), and Matt Crocker (CREAIT—TERRA Facility).

Article information

History dates

Received: 19 October 2022
Accepted: 10 October 2023
Accepted manuscript online: 24 October 2023
Version of record online: 2 January 2024

Copyright

Data availability

Data generated or analyzed during this study are available in the Memorial University data repository (https://doi.org/10.5683/SP3/OJ2JDK).

Author information

Author ORCIDs

M.J. Gill https://orcid.org/0000-0002-4830-8835
K.M. Poduska https://orcid.org/0000-0003-4495-0668
P.L. Morrill https://orcid.org/0000-0002-9169-7063

Author contributions

Conceptualization: MJG, PLM
Data curation: MJG, KMP, PLM
Formal analysis: MJG, KMP, PLM
Funding acquisition: PLM
Investigation: MJG, KMP, PLM
Methodology: MJG, KMP, PLM
Project administration: PLM
Resources: KMP, PLM
Software: KMP
Supervision: PLM
Validation: PLM
Visualization: PLM
Writing – original draft: MJG, KMP, PLM
Writing – review & editing: MJG, KMP, PLM

Competing interests

The authors declare there are no competing interests.

Funding information

This study was supported by grants from Natural Sciences and Engineering Research Council (NSERC) Discovery Grant awarded to PLM, and Natural Sciences and Engineering Research Council Collaborative Research and Development Grant (NSERC CRD) with Nalcor Energy as an industrial partner awarded to PLM.

Supplementary material

Supplementary data are available with the article at https://doi.org/10.1139/cjes-2022-0116.

References

Anderson, L.G. 2013. Carbonate dissolution. *In* Encyclopedia of marine geosciences. *Edited by* J. Harff, M. Meschede, S. Petersen and J. Thiede. Springer, Dordrecht. pp. 132–136.

Barnes, I., and O'Neil, J. 1969. The relationship between fluids in some fresh alpine-type ultramafics and possible modern serpentinization, western United States. Geological Society of America Bulletin, **80**: 1947–1960. doi:10.1130/0016-7606(1969)80%5b1947:TRBFIS%5d2.0.CO;2.

Barnes, I., LaMarche, J., and Himmelberg, G. 1967. Geochemical evidence of present-day serpentinization. Science, **156**: 830–832. doi:10.1126/science.156.3776.830. PMID: 17780302.

Canada, E.a.C.C. 2021. Greenhouse gas emissions: Canadian Evironmental Sustainability Indicators. Government of Canada, G.o. Canada, Gatineau QC

Cook, M.C., Blank, J.G., Rietze, A., Suzuki, S., Nealson, K.H., and Morrill, P.L. 2021. A geochemical comparison of three terrestrial sites of serpentinization: the Tablelands, the Cedars, and Aqua de Ney. JGR Biogeosciences, **126**. doi:10.1029/2021jg006316.

DiPietro, J. 2013. Keys to the interpretation of geological history in landscape evolution in the United States. Elsevier, Amsterdam. pp. 327–344.

Elthon, D. 1991. Geochemical evidence for formation of the Bay of Islands ophiolite above a subduction zone. Letters to Nature, **354**: 140–143.

Frost, B.R., and Beard, J.S. 2007. On Si activity and serpentinization. Journal of Petrology, **48**: 1351–1368. doi:10.1093/petrology/egm021.

Geological Survey of Newfoundland and Labrador 2013. Geoscience Atlas, Version 3 Build 1. Available from https://geoatlas.gov.nl.ca/Default.htm [accessed 10 May 2023].

Giampouras, M., Garrido, C.J., Bach, W., Los, C., Fussmann, D., Monien, P., and García-Ruiz, J.M. 2020. On the controls of mineral assemblages and textures in alkaline springs, Samail Ophiolite, Oman. Chemical Geology, **533**: 119435. doi:10.1016/j.chemgeo.2019.119435.

Girardeau, J., and Nicolas, A. 1981. The structures of two ophiolite massifs, Bay-of-Islands, Newfoundland: a model for the oceanic crust and upper mantle. Tectonophysics, **77**: 1–34. doi:10.1016/0040-1951(81)90159-1.

International Energy Agency. 2023. CO_2 emissions in 2022. Available from https://www.iea.org/reports/co2-emissions-in-2022 [accessed April 2023]

Kelemen, P.B., and Matter, J. 2008. In situ carbonation of peridotite for CO2 storage. Proceedings of the National Academy of Sciences U.S.A., **105**: 17295–17300. doi:10.1073/pnas.0805794105.

Kelemen, P.B., Aines, R., and Bennett, E. 2018. In situ carbon mineralization in ultramafic rocks: natural processes and possible engineered methods. Energy Procedia, **146**: 92–102. doi:10.1016/j.egypro.2018.07.013.

Kelemen, P.B., McQueen, N., Wilcox, J., Renforth, P., Dipple, G., and Vankeuren, A.P. 2020. Engineered carbon mineralization in ultramafic rocks for CO2 removal from air: review and new insights.

Chemical Geology, **550**: 119628–119628. doi:10.1016/j.chemgeo.2020.119628.

Knorr, W. 2009. Is the airborne fraction of anthropogenic CO2 emissions increasing? Geophysical Research Letters, **36**: 1–5. doi:10.1029/2009gl040613.

Morrissey, L.S., and Morrill, P.L. 2017. Flux of methane release and CO2 sequestration at Winterhouse Canyon, Gros Morne, Newfoundland, Canada: a site of continental serpentinization [Article]. Canadian Journal of Earth Sciences, **54**: 257–262. doi:10.1139/cjes-2016-0123.

NOAA. 2020. Trends in atmospheric CO2 [web page dataset]. Available from https://www.esrl.noaa.gov/gmd/ccgg/trends/global.html [accessed October 2020].

Paukert, A.N., Matter, J.M., Kelemen, P.B., Shock, E.L., and Havig, J.R. 2012. Reaction path modeling of enhanced in situ CO2 mineralization for carbon sequestration in the peridotite of the Samail Ophiolite, Sultanate of Oman. Chemical Geology, **330-331**: 86–100. doi:10.1016/j.chemgeo.2012.08.013.

Pogge von Strandmann, P.A.E., Burton, K.W., Snaebjornsdottir, S.O., Sigfusson, B., Aradottir, E.S., Gunnarsson, I., et al. 2019. Rapid CO_2 mineralisation into calcite at the CarbFix storage site quantified using calcium isotopes. Nature Communications, **10**: 1983. doi:10.1038/s41467-019-10003-8. PMID: 31040283.

Podgrajsek, E., Sahlée, E., Bastviken, D., Holst, J., Lindroth, A., Tranvik, L., and Rutgersson, A. 2013. Comparison of floating chamber and eddy covariance measuremnets of lake and greenhouse gas fluxes. Biogeosciences Discussions, **10**: 18309–18335. doi:10.5194/bgd-10-18309-2013.

Pokrovsky, O.S., and Schott, J. 2004. Experimental study of brucite dissolution and precipitation in aqueous solutions: surface speciation and chemical affinity control. Geochimica et Cosmochimica Acta, **68**: 31–45. doi:10.1016/s0016-7037(03)00238-2.

Rudge, J.F., Kelemen, P.B., and Spiegelman, M. 2010. A simple model of reaction-induced cracking applied to serpentinization and carbonation of peridotite. Earth and Planetary Science Letters, **291**: 215–227. doi:10.1016/j.epsl.2010.01.016.

Saldi, G.D., Jordan, G., Schott, J., and Oelkers, E.H. 2009. Magnesite growth rates as a function of temperature and saturation state. Geochimica et Cosmochimica Acta, **73**: 5646–5657. doi:10.1016/j.gca.2009.06.035.

Staal, C.R., Whalen, J.B., McNicoll, V.J., Pehrsson, S., Lissenberg, C.J., Zagorevski, A., et al. 2007. The Notre Dame arc and the Taconic orogeny in Newfoundland. *In* 4-D framework of continental crust. R.D. Hatcher, Jr., M.P. Carlson, J.H. McBride and J.R. Martínez Catalán. Geological Society of America, Boulder, CO. pp. 511–552.

Solomon, S., Plattner, G., Knutti, R., and Friedlingstein, P. 2009. Irreversible climate change due to carbondioxide emissions. Proceedings of the National Academy of Sciences U.S.A., **106**: 1704–1709. doi:10.1073/pnas.0812721106.

Szponar, N., Brazelton, W.J., Schrenk, M.O., Bower, D.M., Steele, A., and Morrill, P.L. 2013. Geochemistry of a continental site of serpentinization, the Tablelands Ophiolite, Gros Morne National Park: a Mars analogue. Icarus, **224**: 286–296. doi:10.1016/j.icarus.2012.07.004.

White, S.K., Spane, F.A., Schaef, H.T., Miller, Q.R., White, M.D., Horner, J.A., et al. 2020. Quantification of CO_2 Mineralization at the Wallula Basalt Pilot Project. Environmental Science & Technology **54**(22): 14609–14616. doi:10.1021/acs.est.0c05142.